Ab–initio Modeling of Physisorption at Metal Surfaces

A van der Waals Density–Functional Study of Benzene Adsorption at Ag(111)

Diplomarbeit von

Falko Axmann

Contents

List of Figures

5

List of Tables

Chapter 1

Introduction

This study concerns the computational modelling of chemical systems, a field which can be traced back to the advent of quantum mechanics when Heitler and London presented a model for atomic binding [2] or the description of the benzene molecule using the LCAO–approach [3] by Hückel [4]. From there, more and more methods have been developed—not without taking advantage of the rise of high performance parallel computing—which not only describe the interaction between atoms, but molecules and crystalline structures of varying degrees of complexity.

One of the most successful methods for a quantitative modeling of chemical binding is density functional theory [5–8] (DFT). This approach moves away from the wave function as the central quantity and makes instead use of the electron density—an ansatz shared with the earlier Thomas Fermi theory [9].

However, the success of DFT lays mainly in describing valence bonds with a short–ranged treatment of electronic exchange and correlation effects, such as generalized–gradient and local–density DFT functionals. As soon as one moves to sparse matter systems, where long range correlation effects such as the van der Waals interaction play a significant role, the performance of standard DFT degrades dramatically. Yet, these systems are of vital importance in several areas of physics, chemistry, but also biology. To name a few, there is the interaction between graphene layers, molecular crystals, water overlayers, DNA, protein folding and, of course, physisorption of molecules at surfaces. The latter is the subject of this study, in particular the adsorption of benzene on a Ag(111) surface. The aim

is not only the qualitative description of the process, but the prediction of experimentally reproducable quantities. For this, a recently developed approach [10] for the integration of long ranged van der Waals interactions into DFT is explored.

Out of the systems named above, the adsorption of Benzene was chosen as a model system for several reasons. Benzene for itself already plays an important role as a starting material in the chemical industry. However, what is more important in the context of this work—where its adsorption is studied—is its model character as an organic molecule. For example, two phenyl rings connected through a nitrogen bridge constitute azobenzene, a molecular switch [11]. Other applications of organic molecules include the use of electroluminescent materials for displays [12].

The advantage of benzene over the use of more complex molecules—such as azobenzene—is its size. Calculations can be performed a lot faster than with larger organics which gives a lot more options to assess the performance of simulation methods and to systematically analyze the influence of various parameters associated with such simulations. Once this has been done, the application of such methods to larger molecules should be a much simpler endeavour.

Chapter 2

Theory

2.1 Density Functional Theory

The approach used in this work to calculate the energy of a given system is based on the Density Functional Theory (DFT). I will thus give a short introduction to it in the following chapter and present some of the techniques used to apply it to surface calculations. Please consult the cited literature for more detailed information.

The basic idea behind DFT is to characterize a given system not using wave functions, but instead via the observable electron density. One advantage of DFT lies in the reduction of the dimensionality of the problem. The N–electron wave function with a dependence on $3N$ spatial and N spin variables is replaced by a density distribution dependent on 3 coordinates. The ground state energy of the system is then expressed as a functional of the electron density $E[n(\mathbf{r})]$ and the minimization of this energy within a self consistent field (SCF) calculation (see figure 2.1) results in the ground state density and energy.

2.1.1 Hohenberg-Kohn theorems

In order to be able to determine all properties of the system using the ground state electron density n_0, the density has to uniquely characterize the Hamiltonian. That this is possible has been proven by Hohenberg and Kohn in a paper published in 1964 [5] and is usually referred to as the first Hohenberg-Kohn Theorem. In

the same paper, they also establish a variational principle according to which the energy functional gives the lowest energy if and only if the electron density is the true ground state density. This is the second Hohenberg-Kohn Theorem.

2.1.2   Kohn-Sham approach

While the two Hohenberg-Kohn theorems show that it is possible to describe a system using the electron density and that the correct density minimizes the total energy of the system, one still requires a method to actually find n. Such a method has been proposed by Kohn and Sham in a paper published in 1965 [6].

The essential idea is to transform the problem of an interacting, inhomogeneous electron gas, moving in a potential $v(\mathbf{r})$ into a system of noninteracting electrons, moving in a potential $v_{\text{eff}}(\mathbf{r})$. This new system can then be described by solving a one-particle Schrödinger equation. Since the potential $v_{\text{eff}}(\mathbf{r})$ depends on the electron density and since the electron density results from the solution of the Schrödinger equation, the whole system has to be solved using an iterative self consistent field (SCF) calculation.

Kohn and Sham derive their theory by starting from the ground-state energy of an interacting, inhomogeneous electron gas in the potential $v(\mathbf{r})$ which can be written as [5]

$$E[n] = \int v(\mathbf{r})n(\mathbf{r})\mathrm{d}\mathbf{r} + \frac{1}{2}\int\int \frac{n(\mathbf{r})n(\mathbf{r}')}{|\mathbf{r}-\mathbf{r}'|}\mathrm{d}\mathbf{r}\mathrm{d}\mathbf{r}' + G[n] \qquad (2.1)$$

where $n(\mathbf{r})$ is the density and $G[n]$ is a universal functional given by

$$G[n] = T_s[n] + E_{xc}[n] \qquad (2.2)$$

with the kinetic energy of a system of noninteracting electrons $T_s[n]$. E_{xc} contains the exchange and correlation energy as well as the difference between $T_s[n]$ and the actual kinetic energy of the system of interacting electrons. The exact form of E_{xc} is unknown, but several approximations exist. For a slowly varying electron density, the exchange correlation functional can be expressed as [5]

$$E_{xc}[n] = \int n(\mathbf{r})\epsilon_{xc}(n(\mathbf{r}))\mathrm{d}\mathbf{r} \; . \qquad (2.3)$$

The energy in equation (2.1) has to be stationary for the correct density $n(\mathbf{r})$ which means that the equation

$$\int \delta n(\mathbf{r}) \left\{ \phi(\mathbf{r}) + \frac{\delta T_s[n]}{\delta n(\mathbf{r})} + \mu_{xc}(n(\mathbf{r})) \right\} \mathrm{d}\mathbf{r} = 0 \qquad (2.4)$$

has to be fulfilled. μ_{xc} and ϕ are given by

$$\phi(\mathbf{r}) = v(\mathbf{r}) + \int \frac{n(\mathbf{r}')}{|\mathbf{r} - \mathbf{r}'|} \mathrm{d}\mathbf{r}' \quad \text{and} \quad \mu_{xc}(n) = \frac{\mathrm{d}(n\epsilon_{xc}(n))}{\mathrm{d}n} \; . \qquad (2.5)$$

Equation (2.4) is the same as one would find for a system of noninteracting electrons [5] in a potential

$$v_{\mathrm{eff}}(\mathbf{r}) = \phi(\mathbf{r}) + \mu_{xc}(n(\mathbf{r})) \; . \qquad (2.6)$$

With this new potential, one obtains a one-particle Schrödinger equation

$$\left\{ -\frac{1}{2}\Delta^2 + v_{\mathrm{eff}}(\mathbf{r}) \right\} \Psi_i(\mathbf{r}) = \epsilon_i \Psi_i(\mathbf{r}) \qquad (2.7)$$

and from its solutions, the density can be calculated:

$$n(\mathbf{r}) = \sum_{i=1}^{N} |\Psi_i(\mathbf{r})|^2 \; . \qquad (2.8)$$

This electron density then results in a new potential v_{eff} which completes the self consistency cycle (see figure 2.1 for a schematic of the process).

2.1.3 Exchange correlation functionals

The quality of the resulting ground state energy depends solely on the chosen exchange correlation functional. Most of these functionals are either based on the local density approximation (LDA) or the generalized gradient approximation (GGA). The basic idea behind both types can be seen by rewriting E_{xc} in terms of an energy density ε_{xc},

$$E_{\mathrm{xc}}^{\mathrm{LDA}} = \int n(\mathbf{r})\varepsilon_{\mathrm{xc}}^{\mathrm{LDA}}[n(\mathbf{r})]\mathrm{d}\mathbf{r} \; . \qquad (2.9)$$

In the case of the LDA, ε_{xc} depends only on the *local* value of n at $\mathbf{r}$. Often, the term *LDA* is not only used for the general approach, but also for a particular functional which is based on the model of a homogeneous electron gas [5].
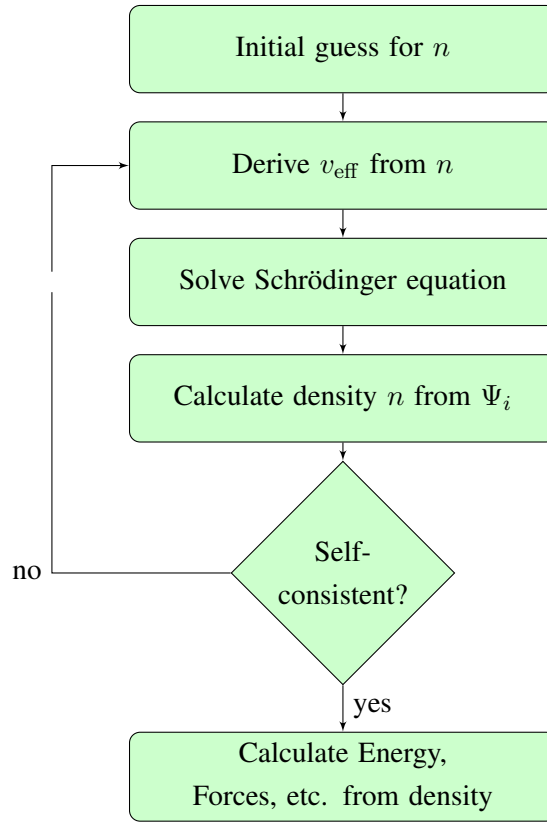
Figure 2.1: Self consistent calculation using the Kohn-Sham ansatz

The results of the LDA can be improved by not only considering the local value of n, but also its gradient ∇n at $\mathbf{r}$. This is then referred to as generalized gradient approximation (GGA) where the XC-energy can be written as

$$E_{\text{xc}}^{\text{GGA}} = \int \mathrm{d}\mathbf{r} f(n, \nabla n) n(\mathbf{r}) \varepsilon_{\text{xc}}^{\text{GGA}}[n(\mathbf{r})] . \qquad (2.10)$$

In practical calculations, ε_{xc} and f are parametrized with analytic functions.

In this work, the GGA functionals PBE [13] and revPBE [14] were used for non-vdW calculations.

The PBE and revPBE functional

The following is just a brief overview of the construction of the two exchange correlation functionals used in this thesis. Please consult the original publications

for the mathematical details of their derivation. The revPBE functional is—as the name suggests—based on the PBE functional.

The correlation part of the PBE functional is obtained by starting from the rather general form

$$E_C^{\mathrm{PBE}} = \int \mathrm{d}\mathbf{r} n[\epsilon_C^{\mathrm{LDA}}(r_s, \zeta) + H(r_s, \zeta, t)] \, . \tag{2.11}$$

with the local Seitz radius r_s, the relative spin polarization $\zeta = (n_\uparrow - n_\downarrow)/n$ and the dimensionless density gradient $t = |\nabla n|/2\phi k_s n$. The gradient contribution H is then obtained by requiring it to fulfil three conditions which describe its limit for the slowly varying, high density case, the rapidly varying case as well as its scaling behaviour. From these conditions, the correlation part of the functional is constructed. The exchange part is constructed from four additional conditions. One of them introduces the parameter κ which is fixed using the local Lieb–Oxford bound [15]. This bound establishes a lower limit for the exchange part of exchange–correlation functionals.

This is where revPBE differs from PBE, κ is there fitted to exact exchange–only total atomic energies. Due to that, the local Lieb–Oxford bound is no longer satisfied for spin–polarized densities, while the weaker integrated Lieb–Oxford bound still holds. Due to this different fitting, the *exchange* part of revPBE does no longer contribute to the binding in cases where the *correlation* part of the functional should be the main origin of the interaction. This aspect will later prove to be of importance for its use together with the vdW–DF functional.

2.2 Van der Waals interactions

2.2.1 Origin of van der Waals interactions

There are various ways in which a molecule can be adsorbed on a surface and they are usually grouped into a chemisorption and physisorption regime. In the former case of chemisorption, the electron densities of the molecule and the surface overlap significantly and a chemical interaction between the adsorbate and the substrate occurs. Physisorption, on the other hand, is characterized by a small overlap of the electron densities with only little disturbance of the adsorbate and

substrate geometries. The primary source for the binding investigated in this thesis is the physisorption due to van der Waals interactions, I will thus give a short overview of the origin of this interaction.

Since the overlap of the electron densities of the adsorbate and the surface is small, both of these densities can in a simplified picture be seen as two separate, unconnected densities. Due to fluctuations in both densities, induced dipoles are formed. The electric field associated with such a dipole is

$$\mathbf{E} = \frac{1}{4\pi\varepsilon_0 R^3}(3p \cdot \cos\theta \cdot \hat{\mathbf{R}} - \mathbf{p}) , \tag{2.12}$$

with the momentary dipole moment $\mathbf{p}$, $\hat{\mathbf{R}}$ being a unit vector pointing in the surface $\rightarrow$ adsorbate direction, and the rotation of the dipole relative to this connection axis denoted as θ. Induced dipoles are oriented so that $\mathbf{p}\|\hat{\mathbf{R}}$ and $\cos\theta = 1$. The resulting electrostatic fields are then

$$\mathbf{E}_{\mathrm{surf}} = \frac{2p_{\mathrm{surf}}}{4\pi\varepsilon_0 R^3}\hat{\mathbf{R}}, \qquad \mathbf{E}_{\mathrm{ads}} = \frac{2p_{\mathrm{ads}}}{4\pi\varepsilon_0 R^3}\hat{\mathbf{R}} . \tag{2.13}$$

Each of these fields then induces a dipole in the opposite electron density which depends on the polarizability α,

$$\mathbf{p}_{\mathrm{surf}}^{\mathrm{ind}} = \alpha_{\mathrm{surf}} \cdot \mathbf{E}_{\mathrm{ads}}, \qquad \mathbf{p}_{\mathrm{ads}}^{\mathrm{ind}} = \alpha_{\mathrm{ads}} \cdot \mathbf{E}_{\mathrm{surf}} . \tag{2.14}$$

The potential energy between the two dipoles is given by

$$E_{\mathrm{pot}}(R) = -\mathbf{p}_{\mathrm{surf}}^{\mathrm{ind}} \cdot \mathbf{E}_{\mathrm{ads}} = -\mathbf{p}_{\mathrm{ads}}^{\mathrm{ind}} \cdot \mathbf{E}_{\mathrm{surf}} . \tag{2.15}$$

After substituting $\mathbf{p}_{\mathrm{surf}}^{\mathrm{ind}}$ and $\mathbf{p}_{\mathrm{ads}}^{\mathrm{ind}}$ from eq. (2.14), one obtains

$$E_{\mathrm{pot}}(R) \propto -\mathbf{p}_{\mathrm{surf}}^{\mathrm{ind}} \cdot \mathbf{p}_{\mathrm{ind}}^{\mathrm{surf}} \Rightarrow E_{\mathrm{pot}}(R) = -C_1\frac{\alpha_{\mathrm{surf}} \cdot \alpha_{\mathrm{ads}}}{R^6} . \tag{2.16}$$

While this model is only a very simple one, it already explains the asymptotic R^{-6} dependence one finds in some of the approaches used to integrate vdW interactions into DFT.

2.2.2 Approaches for integrating vdW-interactions into DFT

There are multiple approaches for taking van der Waals interactions into account within the DFT framework. One such scheme was proposed by Wu and Yang [16]

and Grimme [17] and is based on adding an empirical potential of the form $C_6 R^{-6}$ to the DFT energy with the interatomic distances R and the dispersion coefficients C_6. Thus, the correction is not directly based on the electron density, but rather on the (usually optimized) positions of the atom cores. The dispersion corrected total energy is then

$$E_{\text{DFT}} = E_{\text{DFT}} + E_{\text{disp}} \tag{2.17}$$

with the DFT energy E_{DFT} obtained using a short–ranged xc–functional and the empirical dispersion correction E_{disp} given by

$$E_{\text{disp}} = -s_6 \sum_{i=1}^{N-1} \sum_{j=i+1}^{N} \frac{C_6^{ij}}{R_{ij}^6} f_{\text{dmp}}(R_{ij}) \,. \tag{2.18}$$

Here, s_6 is a global scaling factor, N denotes the number of atoms in the system, C_6^{ij} is the dispersion coefficient for atom pair ij and R_{ij} is the interatomic distance. A damping function f_{dmp} is used to limit the correction to long ranged effects at large R.

While the former approach uses C_6 coefficients which are based on experimental values [16], a scheme was proposed by Tkatchenko and Scheffler [18] which determines the required parameters from the DFT ground-state electron density.

Since these methods are only based on a pairwise potential, they do not account for effects such as electronic screening, but have the advantage of low computational complexity.

A different approach is the vdW-DF functional which is a non-local functional of the electron density. It is further described in the next section.

2.3 vdW-DF functional

In this work, the scheme proposed by Dion, Langreth and Lundqvist is used to account for vdW interactions. It was initally developed for layered systems [19, 20] but was then extended to general geometries [10].

The van der Waals density functional approximates only the correlation part of the exchange-correlation energy and has thus to be combined with an additional functional for the exchange energy as shown in equation (2.19). This additional functional must not produce a binding which would not be present if the exchange

was treated exactly [21].

$$E_{\mathrm{xc}}[n] = E_{\mathrm{x}}[n] + E_{\mathrm{c}}[n] \, . \tag{2.19}$$

In the original work published by Dion et al., $E_x[n]$ is taken from a GGA functional such as revPBE.

The correlation functional is again divided into two parts,

$$E_c[n] = E_c^0[n] + E_c^{\mathrm{nl}}[n] \, . \tag{2.20}$$

E_c^0 approaches the LDA in the limit of a slowly varying electron gas, while E_c^{nl} contains most nonlocal and longest range terms which yield the van der Waals interaction and vanishes in the LDA limit. The seamless transition between the two limits was one of the challenges in the construction of a working functional. Due to the different range of both terms, different approximations can be used. Since E_c^{nl} accounts for the longest range interactions, it should be less sensitive to details of the system's dielectric response allowing for simple approximations for the dielectric function. E_c^0 on the other hand is approximated using the LDA. That way, one can make use of the accuracy of the LDA for short range/high density parts of the system while finding a better approximation for the long range domain.

E_c^{nl} can be written as:

$$E_c^{\mathrm{nl}} = \frac{1}{2} \int \mathrm{d}\mathbf{r} \int \mathrm{d}\mathbf{r}' n(\mathbf{r}) \phi(\mathbf{r}, \mathbf{r}') n(\mathbf{r}') \, . \tag{2.21}$$

$\phi(\mathbf{r}, \mathbf{r}')$ is some given, general function depending on $(\mathbf{r} - \mathbf{r}')$ and the density n.

2.3.1   Derivation of the kernel ϕ

In the section above, the challenge of finding a full exchange–correlation functional was reduced to finding a non–local correlation functional accounting for the longest range interactions only. The other contributions to the full functional are taken from known LDA and GGA functionals. In the following text, the non–local correlation part E_c^{nl} will be derived. In the domain of long–range interactions, the system's sensitivity to details of the dielectric response is much smaller than for short–range interactions. Thus it makes sense to express the non–local exchange–correlation energy by a simple approximation for the dielectric function. This can be done using the adiabatic connection formula.

Adiabatic connection formula

One can find an integral expression for the exchange–correlation energy by looking at a slightly modified, fictitious system, where the electron–electron Coulomb interaction can be continuously turned on and off:

$$H^\lambda = T + V_{\text{eff}}^\lambda + \lambda V \ . \tag{2.22}$$

The effective local potential V_{eff}^λ is chosen so that the resulting ground–state density corresponds to the real ground–state density for any λ. For $\lambda = 1$, the effective potential becomes the external potential V_{ext}. The total energy of the system can now be expressed in terms of an integral over λ:

$$E = T_s + V_{\text{ext}} + \int_0^1 \mathrm{d}\lambda \langle \psi^\lambda | V | \psi^\lambda \rangle \ . \tag{2.23}$$

The last term contains the Hartree as well as the exchange–correlation energy. The latter can be split off by rewriting the expression in terms of the electron pair density. We then obtain E_{xc} as a functional of the electron density n and the exchange–correlation hole n_{xc} [22]:

$$E_{\text{xc}} = \int \mathrm{d}\lambda \ \mathrm{d}^4x \ \mathrm{d}^4x' \frac{n(\mathbf{x}) n_{\text{xc}}^\lambda(\mathbf{x}, \mathbf{x}')}{|\mathbf{r} - \mathbf{r}'|} \ . \tag{2.24}$$

Here, $\mathbf{x}$ also contains the temporal coordinate, while $\mathbf{r}$ is only the positional part of $\mathbf{x}$.

The fluctuation–dissipation theorem allows us to relate fluctuations to response functions [23] and to further rewrite E_{xc}:

$$E_{\text{xc}} = -\int_0^1 \frac{\mathrm{d}\lambda}{\lambda} \int_0^\infty \frac{\mathrm{d}u}{2\pi} \mathrm{Tr}[\chi_\lambda V_\lambda] - E_{\text{self}} \ . \tag{2.25}$$

u is an imaginary frequency replacing the time variable of χ_λ and V_λ is the inter–electron Coulomb potential scaled by λ, thus $V_\lambda = \lambda/|\mathbf{r} - \mathbf{r}'|$. The self–interaction energy is given by $E_{\text{self}} = \int \mathrm{d}\mathbf{r} \ n(\mathbf{r}) V(0)$. χ_λ describes the density response of the system to an *external* potential $\delta\phi_{\text{ext}}$:

$$\delta n = \chi \ \delta\phi_{\text{ext}} \ . \tag{2.26}$$

Full potential approximation

Our aim is the expression of the exchange–correlation energy in terms of the dielectric function ϵ, which can be related to the response function $\tilde{\chi}$:

$$\tilde{\chi} = \nabla \frac{\epsilon - 1}{4\pi} \nabla \ . \tag{2.27}$$

The response function $\tilde{\chi}$ describes the density response of the system to the *total* (screened) potential $\delta\phi$ as opposed to eq. (2.26) which describes the response to an *external* potential.

   If we could relate χ to $\tilde{\chi}$, we could also express eq. (2.25) in terms of ϵ. The general relation is

$$\chi_\lambda = \tilde{\chi}_\lambda + \tilde{\chi}_\lambda V_\lambda \chi_\lambda \tag{2.28}$$

The exact λ–dependence of $\tilde{\chi}$ is not known. Instead, the full potential approximation [22] (FPA) according to which $\tilde{\chi}_\lambda \approx \tilde{\chi}_{\lambda=1}$ is used. This approximation is exact for longest range vdW interactions and allows the coupling constant integration in eq. (2.25) to be performed, giving

$$E_{\text{xc}}^{\text{FPA}} = \int_0^\infty \frac{\mathrm{d}u}{2\pi} \text{Tr}[\ln(1 - \tilde{\chi}V)] - E_{\text{self}} \ . \tag{2.29}$$

Replacing $\tilde{\chi}$ with the relation from eq. (2.27) we obtain

$$E_{\text{xc}}^{\text{FPA}} = \int_0^\infty \frac{\mathrm{d}u}{2\pi} \text{Tr}[\ln(-\frac{1}{4\pi} \nabla \ \epsilon \ \nabla V)] - E_{\text{self}} \ . \tag{2.30}$$

where $\nabla^2 V = -4\pi$ was used.

The non–local part of E_{xc}

The FPA fails for short ranged interactions and our aim is to split the exchange–correlation energy into two terms (see eq. (2.20)), one accounting for short ranged interactions which will be approximated using the LDA, and one term for the long ranged interactions, which will be derived from eq. (2.30) above.

   The local part of eq. (2.30) is the energy for the homogeneous electron gas:

$$E_{\text{xc}}^{\text{FPA}-\text{local}} = \int_0^\infty \frac{\mathrm{d}u}{2\pi} \text{Tr}[\ln(\epsilon)] - E_{\text{self}} \ . \tag{2.31}$$

Subtracting it from eq. (2.30) gives—after some rearranging—the non–local part of the correlation energy:

$$E_{\mathrm{c}}^{\mathrm{nl}} = \int_0^\infty \frac{\mathrm{d}u}{2\pi} \mathrm{Tr} \left[\ln \left(1 - \left(1 - \frac{1}{\epsilon} \right) - \frac{\tilde{\chi}}{\epsilon} V \right) \right] . \tag{2.32}$$

This expression can now be further approximated to bring it into the form of eq. (2.21).

Plasmon pole approximation

The logarithm in equation (2.32) can be expanded in terms of the quantity $S = 1 - 1/\epsilon$:

$$E_{\mathrm{c}}^{\mathrm{nl}} = \int_0^\infty \frac{\mathrm{d}u}{2\pi} \mathrm{Tr} \left[S^2 - \left(\nabla \cdot S \nabla \frac{-V}{4\pi} \right)^2 \right] . \tag{2.33}$$

From there on a plasmon pole approximation can be used to further simplify the expression for $E_{\mathrm{c}}^{\mathrm{nl}}$.

The general form of S is taken to depend on the electron plasma dispersion function ω_q. This dispersion function is influenced by two types of excitations: One is the electron–hole pair where a single electron is excited above the Fermi surface. The other one results from a collective motion of the electron gas which makes it a long wavelength excitation. The latter is called a plasmon.

For small q, the dispersion function ω_q is dominated by the plasmon contribution, while it scales with q^2 for larger q. We can thus approximate ω_q by constructing a function which interpolates between the ω_p and the q^2 case. Using such an approximation allows us to write S—while respecting the symmetry constraint—in the form

$$S_{\mathbf{q},\mathbf{q}'} = \frac{1}{2} \left[\tilde{S}_{\mathbf{q},\mathbf{q}'} + \tilde{S}_{-\mathbf{q}',-\mathbf{q}} \right] \tag{2.34}$$

where

$$\tilde{S}_{\mathbf{q},\mathbf{q}'} = \int \mathrm{d}\mathbf{r} \, \mathrm{e}^{-\imath(\mathbf{q}-\mathbf{q}')\cdot\mathbf{r}} \frac{\omega_p(\mathbf{r})}{[\omega + \omega_q(\mathbf{r})][-\omega + \omega_{q'}(\mathbf{r})]} \tag{2.35}$$

Using this definition of S allows us to simplify eq. (2.33) and transform it into the form of eq. (2.21). The final definition of the kernel can be found in ref. [10].

Asymptotic limit and C_6 coefficients

The asymptotic behavior of the functional as well as the C_6 coefficients obtained from it can give a first impression of the quality of the approximations used.

It was found [10] that the asymptotic R^{-6} form is correctly reproduced. However, comparing the results for the C_6 coefficients with exact electrodynamics yields an error on the level of 20%.

Chapter 3

Methods

While the choice of the exchange–correlation functional determines the accuracy that can in principle be reached with the DFT calculation, there are several other —technical—parameters that influence the accuracy from the numerical side. All the latter parameters need to be tested in detail to ensure numerical convergence of the calculation.

The basis set used to solve the Kohn–Sham equations (2.7) is one of these additional choices. For example for molecular calculations, atom centered orbitals would be one option. If one wants to simulate crystalline solids, one can make use of their periodic structure by employing plane–waves as basis set (see section 3.2.1). They can also be used for systems containing periodic and non–periodic structures (molecules at a surface) by using supercell geometries (see section 3.1).

3.1 Supercells

For crystalline solids, it is an obvious choice to use unit cells that contain the basic geometry of the solid, together with periodic boundary conditions. However, how does one proceed when dealing with a system that is only partially periodic, such as a surface? This is where supercells come into play.

Supercells are similar to normal unit cells in that periodic boundary conditions are used in each of the three dimensions. To arbitrarily remove unwanted periodicity in one or more directions, vacuum gaps are introduced. The width of such a gap then has to be carefully chosen as to make sure that all unwanted interactions

between the periodic images are removed.

3.1.1   Surface calculations

An example for the use of supercells are surface calculations. Here, slabs built of several layers of atoms are used (see figure 3.1) which are separated by a vacuum region. Both, the slab thickness and the width of the vacuum region have then to be tested for convergence. If the slab was too thin, one would not be able to simulate the properties of the surface of an underlying, infinitely extended bulk. The width of the vacuum gap is important to eliminate unwanted interactions between the periodically repeated slabs.
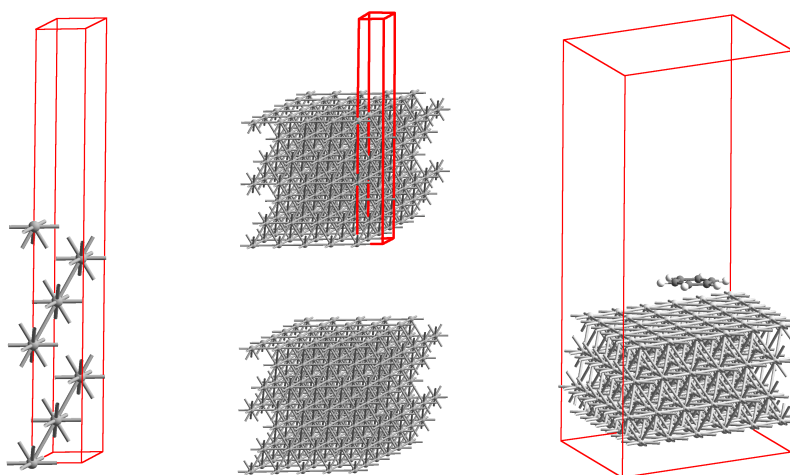
Figure 3.1: A single supercell of a surface (left) and the same supercell with some of its periodic images (middle). The supercell on the right is used for adsorption energy calculations.

The optimised lattice constant which is used for the construction of the slab is obtained from bulk calculations (see section 4.1).

When adsorption processes are analysed, it is important to shield the adsorbate against lateral interactions with its periodic images. This is done by creating a larger surface area within the supercell at which the adsorbate is placed. The size of this surface area is then also subject to convergence tests.

3.2 Plane wave basis sets and pseudopotentials

3.2.1 Plane waves

The Kohn-Sham equations (2.7) are solved by expanding them into a set of basis functions. In this work, plane waves were used as they are particularly well suited for periodic systems.

Each of the plane waves has a wave vector $\mathbf{k}$ which lies within the Brillouin zone and, together with a band index j, characterizes each wave function $\psi_{\mathbf{k}j}(\mathbf{r})$. The foundation to this lies in Bloch's theorem, stating that the wave functions can be expanded into a Fourier series:

$$\psi_{\mathbf{k}j}(\mathbf{r}) = \sum_{\mathbf{G}} c_{\mathbf{G}}^{\mathbf{k}j} e^{i(\mathbf{k}+\mathbf{G})\mathbf{r}} \ . \tag{3.1}$$

The sum runs over all reciprocal lattice vectors $\mathbf{G}$. Wave functions which lie close together in terms of $\mathbf{k}$ are similar which can be used to solve the Kohn-Sham equations (2.7) using a discrete number of plane waves, each with a different $\mathbf{k}$. The number of k-points can often be further reduced due to symmetries. The k-point sampling scheme used in this work has been proposed by Monkhorst and Pack [24] and the resulting k-point distribution is usually referred to as MP-Grid. This k-point mesh needs to be tested for convergence, i.e. it needs to be increased until the targeted quantities are converged to the desired accuracy.

By expressing the Kohn-Sham equation in the notation of Bloch-states, one obtains

$$\left(-\frac{\hbar^2}{2m}\Delta + V_{\text{eff}}(\mathbf{r})\right)\psi_{\mathbf{k}j}(\mathbf{r}) = \varepsilon_{\mathbf{k}j}\psi_{\mathbf{k}j}(\mathbf{r}) \ . \tag{3.2}$$

This can be transformed into a matrix eigenvalue equation using (3.1) and several transpositions [25]:

$$\sum_{\mathbf{G}}\left(\frac{\hbar^2}{2m}\|\mathbf{k}+\mathbf{G}\|^2\delta_{\mathbf{G}\mathbf{G}'} + V_{\text{eff}}(\mathbf{G}-\mathbf{G}')\right)c_{\mathbf{G}}^{\mathbf{k}j} = \varepsilon_{\mathbf{k}j}c_{\mathbf{G}'}^{\mathbf{k}j} \ . \tag{3.3}$$

Here, $\frac{\hbar^2}{2m}\|\mathbf{k}+\mathbf{G}\|^2$ corresponds to the kinetic energy of the plane wave. In practical calculations this energy is limited by truncating the fourier expansion (3.1) at a kinetic energy cutoff, so that

$$\frac{\hbar^2}{2m}\|\mathbf{k}+\mathbf{G}\|^2 \leq E_{\text{cutoff}} \ . \tag{3.4}$$

In this work, the choice of the kinetic energy cutoff is a very important convergence criterium. Since E_{cutoff} influences the resolution of plane waves in the reciprocal space, it also changes the precision of the grid with which the electron density can be sampled in real space. The vdW calculations performed in this work rely on a post processing step that is solely based on the electron density produced by DFT calculations, thus its resolution can have a wide impact (see below).

3.2.2   Pseudopotentials

Closely connected to plane wave DFT is the use of pseudopotentials as these potentials reduce the number of plane waves required. The rapidly varying wave functions of the core electrons would normaly require a high kinetic energy cutoff to be properly represented by plane waves. At the same time, their effect on chemical bonds is very small as core electron wave functions from one atom usually don't overlap with those from neighboring atoms. This is where pseudopotentials are used to replace the potential of the core electrons (and the core itself) with a new potential [25]. This new potential has to be constructed in a way that won't change the valence wave functions, which reduces its effect on the chemical characteristics of the atom.

3.3   Surface energy

The surface energy is the energy required to form a surface from a solid body. While the computation of surface energies is not the main focus of this thesis, it still gives some insight into how such quantities are generally calculated via DFT.

Such a calculation is divided into two parts: One DFT calculation for the bulk energy E_{bulk} and another one with a supercell containing n layers of the bulk unit cell as well as vacuum to form a surface and the resulting energy E_{surf}. Such a simulation is described in section 4.2.

The surface energy of a (111) surface is defined as energy per surface area, so the area of a unit cell has to be determined. For a unit cell with cell vectors of

equal length ν, it is given by $A_\mathrm{u} = \nu^2 \cdot \frac{\sqrt{3}}{2}$. The surface energy σ is then

$$\sigma = \frac{1}{2} \cdot \frac{E_\mathrm{surf} - nE_\mathrm{bulk}}{A_\mathrm{u}} = \frac{1}{2} \cdot \frac{2(E_\mathrm{surf} - nE_\mathrm{bulk})}{\nu^2\sqrt{3}} = \frac{1}{2} \cdot \frac{4(E_\mathrm{surf} - nE_\mathrm{bulk})}{a_0^2\sqrt{3}} \quad (3.5)$$

The factor $\frac{1}{2}$ was introduced as the supercell approach does not result in one, but actually two surfaces, since the surface slab has two sides.

3.4 Adsorption energy

The adsorption energy is the energy that is gained by the system upon adsorption. A negative energy reflects that the adsorption process is exothermic.

The scheme with which the adsorption energy is calculated is very similar to how the surface energy was determined in section 3.3. The calculation is based on the following energies/geometries:

- E_at: The adsorbate located at the surface.

- E_surf: The clean surface.

- E_gas: The gas phase geometry of the adsorbate.

The adsorption energy is then given by

$$E_\mathrm{ads} = E_\mathrm{at} - (E_\mathrm{surf} + E_\mathrm{gas}) \, . \quad (3.6)$$

3.5 The JuNoLo program

The calculation of total energies in this study is performed in two steps: A plane–wave DFT calculation using a short–ranged GGA functional, for which the program "Castep" [26] was used, and a vdW-DF calculation for which the JuNoLo program was used. Applying the vdW-DF calculation as a post-DFT correction instead of a self-consistent calculation is mostly sufficient [27] and that is also how the vdW-DF functional will be applied in this study. The electron density resulting from a DFT calculation with a functional such as PBE will then serve as input for the next step. See figure 3.2 for a simplified flowchart of how JuNoLo works. Since JuNoLo uses only real space, it does work without any periodicity.
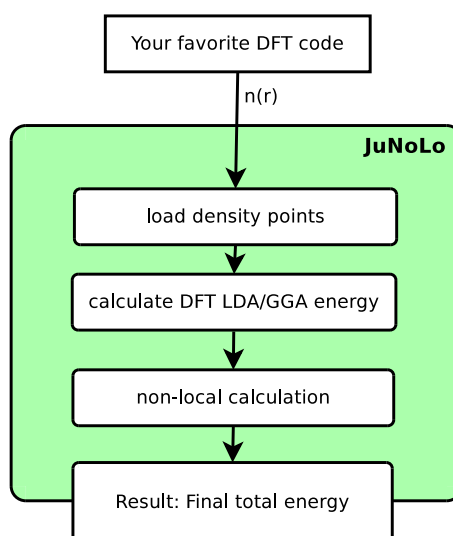
Figure 3.2: JuNoLo Flowchart

If periodicity was required, one could specify a certain number of repetitions for each dimension separately.

To increase speed, it is possible to have JuNoLo ignore some of the density points if the density is lower than a certain threshold. This is known as density trimming.

3.6   Convergence tests

Each numerical calculation can depend on various parameters which do not describe the physical system, but only influence the algorithm and precision used for the simulation. To obtain physically correct, converged results, one has to make sure that the influence of these parameters on the result is sufficiently reduced. One also has to keep in mind that the computational complexity (and with that the runtime required for the calculation) increases with the precision.

Typical convergence parameters for plane wave DFT include the choice of k-points and the kinetic energy cutoff (see section 3.2). For supercell calculations additional parameters are slab thickness and vacuum thickness. Another parameter, which is especially of importance for metallic systems, is the so called smearing width which is explained in the section below.

During a convergence test, the parameter of which the influence is tested is varied over multiple calculations. The results of each calculation are then compared. If the difference between two successive tests is below a certain limit—which then forms the error margin of the result—the parameter is considered to be converged at that point.

Smearing

At zero temperature, the density of states for a metal is discontinuous at the point where the energy crosses the Fermi surface. Due to the finite number of k-points used for integrations over the Brillouin zone, this can lead to sampling inaccuracies. One would then have to use a very high number of k-points to exactly sample the Fermi surface. To avoid this computationally demanding task, an artificial, finite temperature is introduced for the electrons. This is done by substituting the exact density of states

$$n(\varepsilon) = \sum_{i\mathbf{k}} \delta(\varepsilon - \varepsilon_{i\mathbf{k}})$$

with a smoother (smeared) density of states

$$n(\varepsilon) = \sum_{i\mathbf{k}} \frac{1}{\sigma} \delta' \left(\frac{\varepsilon - \varepsilon_{i\mathbf{k}}}{\sigma} \right) \ .$$

With δ' being a broadened approximation of the Dirac's delta. The magnitude of this broadening is the smearing width.

Chapter 4

Results

Most of the calculations in this study are a two step process. First, a self–consistent DFT calculation is performed using the PBE exchange–correlation functional. For this, the program Castep [26] is used. The electron density resulting from this first calculation is then used as input for a second non–selfconsistent calculation to obtain the vdW-DF energy correction. For this, the JuNoLo [28] program is used.

Since the Castep results build the basis for the vdW-DF correction, it is only natural to start by assessing its convergence behaviour. This has been done in section 4.1 and 4.2.

4.1   Lattice constant of copper

Before any more complex simulations with surfaces can be done, one first has to know the structure of the bulk. For this, the lattice constant was determined by doing multiple DFT calculations. Each of them used a different lattice constant for the construction of the unit cell. The resulting energies are shown in figure 4.1. The final lattice constant is determined by fitting the Murnaghan equation [29] to the data points and taking its minimum. The absolute energies shown do not have any physical meaning, due to the use of pseudopotentials which add an unknown offset to the total energy. Luckily, we are only interested in the minimum of the curve, not in the absolute energies. The corresponding convergence tests are shown in figure 4.2. Sufficiently converged results required a kinetic energy cutoff of $300\,\mathrm{eV}$. The smearing width was set to $80\,\mathrm{meV}$ and the exchange correlation

functional used was PBE. With these settings, a lattice constant of $a_0 = 3.63\,\text{Å}$ was obtained which is the same result one finds in other literature [30] on PBE–based bulk calculations.
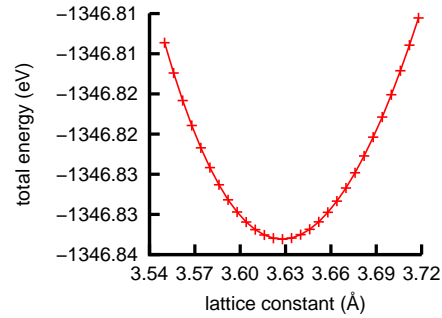
Figure 4.1: Total bulk energy for different lattice constants.
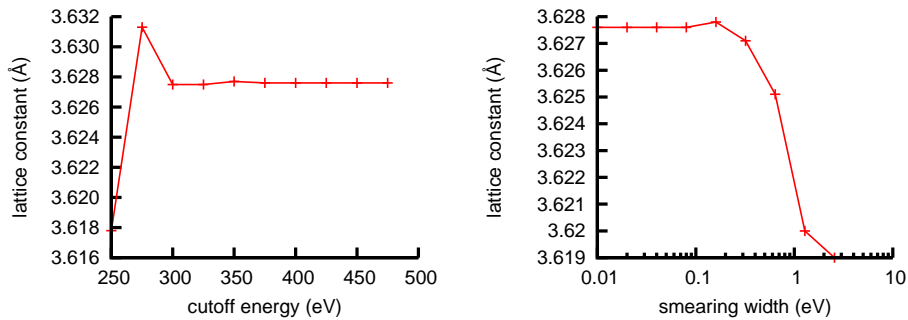
Figure 4.2: Convergence of the copper lattice constant concerning kinetic energy cutoff and smearing width.

4.2 Surface energy

Going up the complexity ladder from a bulk system, the next step is to simulate a surface and determine the associated surface energy as well as the forces acting on the top layer. For this, a supercell containing a surface slab geometry was constructed (for an explanation on what supercells are, see section 3.1).

4.2.1 Supercell geometry

A model of a clean (111) surface was constructed in a supercell containing multiple layers of atoms—the so called slab—and a vacuum region which is required to prevent interactions between the periodically repeated images of the slab. This approach introduces two convergence parameters: The number of layers used for the slab required to simulate not just a thin sheet of metal, but the surface of a (semi–infinite) solid body, and the width of the vaccuum required to avoid unwanted interactions between consecutive slabs.

Surface construction

The surface slab was constructed using four vectors. Two vectors, $\mathbf{a}_1$ and $\mathbf{a}_2$ span the base of the unit cell. The atom offset between the slab layers is given by $\mathbf{a}_3$ and the height of the supercell by $\mathbf{a}_4$ (see figure 4.3b for a schematic).
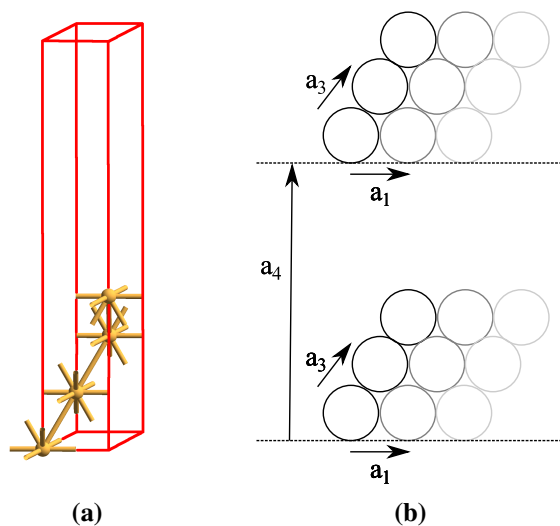

(a)   **(b)**

Figure 4.3: (a) is one of the supercells used for surface calculations. (b) shows how the (111) surface slab was constructed, see the text for details.

The length of the vectors $\mathbf{a}_{1,2,3}$ is $v = \frac{a_0}{\sqrt{2}}$ with the lattice constant a_0. They

are then given by

$$\mathbf{a}_1 = \begin{pmatrix} 1 \\ 0 \\ 0 \end{pmatrix} \cdot v; \quad \mathbf{a}_2 = \begin{pmatrix} \cos(60°) \\ \sin(60°) \\ 0 \end{pmatrix} \cdot v; \quad \mathbf{a}_3 = \begin{pmatrix} 1/2 \\ 1/2\sqrt{3} \\ \sqrt{2/3} \end{pmatrix} \cdot v \quad (4.1)$$

The derivation is quite simple. One takes the three vectors spanning the fcc unit cell and rotates them so that two of them lie in the x/y plane with the third one pointing into the direction of the next layer. This also explains the origin of the $60°$ angles, as these are the angles between the fcc unit cell vectors. The interlayer distance is thus $\frac{\sqrt{2}}{\sqrt{3}} \frac{1}{\sqrt{2}} a_0 = \frac{a_0}{\sqrt{3}}$. Vector $\mathbf{a}_4$ determines the height of the supercell and with that the width of the vacuum, its first two components are zero.

4.2.2   Convergence tests

The results obtained in this section have to be converged concerning several numerical and physical parameters. For this, convergence tests were performed. Each point in these calculations is the result of multiple SCF iterations with which the Kohn-Sham equations are solved. For the tests presented in this section, the SCF cycle was repeated until the resulting forces were determined with a precision of $0.01 \, \mathrm{eV}/\mathrm{\mathring{A}}$ and the energy with a precision of $10^{-8} \, \mathrm{eV}$.

These values are usually far smaller than the error introduced by the chosen cutoff, number of k-points or other factors. This can be seen in figure 4.4. While a kinetic energy cutoff of $400 \, \mathrm{eV}$ gives quite precise results for the surface energy σ, the error margin (compared to the results at $500 \, \mathrm{eV}$) is still way larger than the limits used for the SCF cycles. At the same time, one can see that the smearing width has almost no impact on the surface energy, and only little impact on the force acting on the top layer. Thus a smearing width of $80 \, \mathrm{meV}$ is sufficient.

The number of k-points, which was investigated in the next tests (see figure 4.5), is the number of points in the irreducible brillouin zone (IBZ). The reduction in points comes from the fact that the symmetry of a crystal can be used to reduce the number of calculations in reciprocal space. Here, as in the previous test, the smearing width has only little impact. With 90 k-points giving sufficiently good results (they correspond to a $18 \times 18 \times 1$ Monkhorst–Pack grid).

One important, though more technical, aspect about the choice of the k-point grid is its influence on parallel computing. The calculations are usually distributed

over a network of multiple computers and it is preferable to have each computer node work on an integral number of k-points. Splitting one k-point calculation over multiple nodes would result in increased network traffic and thus slow down the program. To prevent this, it is advantageous to use an even number of k-points in the IBZ which means that the Γ point is not included in the used k-point grids. To make sure that this does not have any negative consequences on the result, an additional tests with and without the Γ point were performed. The result is shown in figure 4.6.
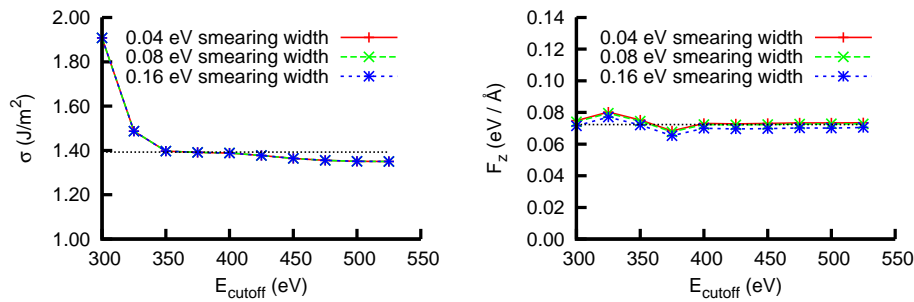
Figure 4.4: Convergence of the surface energy (left) and the top-layer-force (right) as a function of the kinetic energy cutoff.
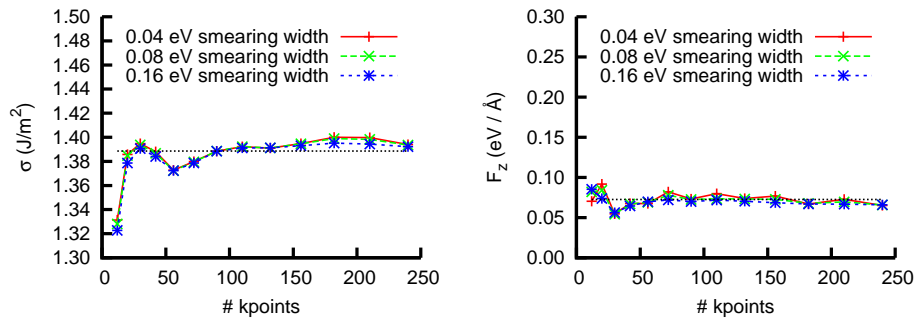
Figure 4.5: Convergence of the surface energy (left) and the top-layer-force (right) as a function of the number of k-points.

With these parameters ($400\,\mathrm{eV}$ cutoff, 90 k-points, $80\,\mathrm{meV}$ smearing width), further tests were performed to determine the required width of the slab and the vacuum (see figure 4.7). This is important as interactions between the periodic images of the slab have to be avoided and since the slab has to be thick enough to

Figure 4.6: Convergence behavior of the surface energy with and without Γ point.

simulate not just a thin metal film, but the surface of a solid object. For technical reasons, the width of the vacuum has been measured in layers with each layer corresponding to the interlayer distance in the slab which is $2.09\,\text{Å}$.

While the influence of the vacuum width is almost non existent, it requires four slab layers for the force acting on the top layer to be sufficiently converged.

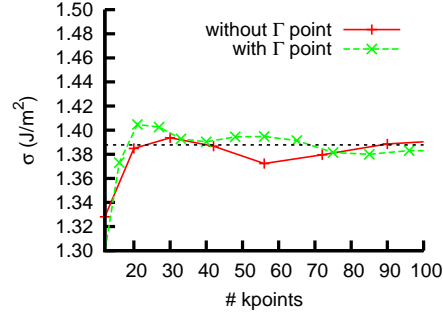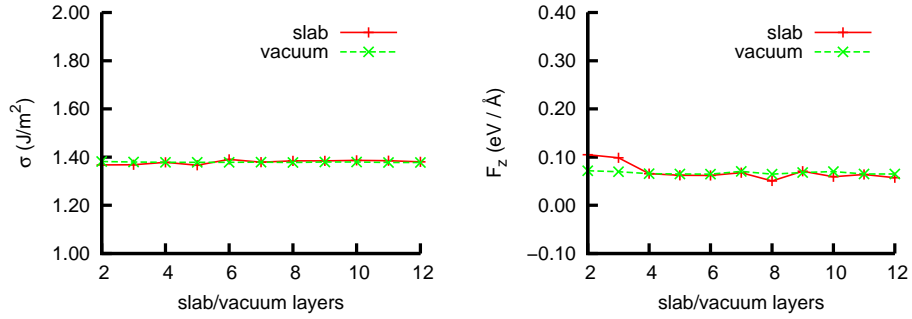**Figure 4.7:** Convergence of the surface energy (left) and the top–layer–force (right) as a function of the slab/vacuum width. For technical reasons, the vaccum width was measured in number of slab layers. The inter–layer spacing was $2.09\,\text{Å}$.

The final result for the surface energy and the force is

$$\sigma = 1.38\,\text{J/m}^2 \qquad F_z = 0.06\,\text{eV}/\text{Å} \ .$$

The surface energy found in the literature [30] is $1.41\,\text{J/m}^2$.

4.2.3 Surface relaxation

As one might expect from the observation that F_z is not zero, the top atom layer—and possibly also lower layers—do not stay at their bulk position. This effect might introduce errors in calculations that only use a truncated bulk structure to form the surface. To evaluate its magnitude, a geometry optimization was performed using the DFT program. During such an optimization, the geometry is altered until the forces acting on each atom are lower than a certain limit (in this case, this limit was $0.01\,\mathrm{eV/\,\text{Å}}$). For this test a slab with 16 atom layers was used with positions of the central two atom layers fixed. This is required to simulate a solid bulk structure underneath the surface. It is also important to fix the central layers instead of just fixing the lower ones. Otherwise, the movement of the atoms on the non-constrained side of the slab can create dipoles which would negatively influence the calculation. The resulting position shifts (in relation to the original layer distance) are shown in table 4.1. The observed changes are so small, that no

	Change in inter–layer distance (%)
d_{12}	-0.79
d_{23}	-0.25
d_{34}	0.18
d_{45}	0.15
d_{56}	0.16
d_{67}	-0.03
d_{78}	0.00

Table 4.1: Change in inter–layer distance for a relaxed Cu–surface compared to the bulk structure.

negative impact on further calculations is to be expected. It is thus sufficient to use an unrelaxed bulk structure for the adsorption calculations.

It should also be noted, that the change in inter–layer distance is not the only possible difference between bulk and surface geometry as additional surface reconstruction [31] can be observed, such as for the Au(111) surface [32]. Very large supercells are required to observe such reconstructions. Fortunately, the here studied Ag(111) surface does not undergo any such reconstruction.

4.3 Adsorption energy of benzene at Ag(111)

The main subject of this thesis is the assesment of the adsorption energy of benzene at a Ag(111) surface under consideration of vdW interactions.

The required calculations have been split into two parts (see section 3.5 for more information) with the normal GGA-DFT step being computed using Castep [26] using the PBE [13] functional. This also includes the geometry optimizations which were performed for the gas phase, as well as for the adsorbed benzene molecule.

The energies obtained from GGA were then corrected in a post–processing step using the program JuNoLo [28]. This program not only derives the vdW-DF energy, but also calculates the PBE and revPBE [14] exchange and correlation energies based on the electron density it receives as input. It was thus possible to obtain not only PBE based, but also revPBE based adsorption energies by subtracting the PBE energy from the GGA calculations and adding the corresponding revPBE energy back. However, the geometry could only be optimized using PBE.

4.3.1 Geometries used

Adsorption site

TPD measurements [1] and cluster model calculations [33] identified two possible adsorption sites for benzene on Ag(111) with the benzene molecule of one configuration rotated by $30°$ with respect to the other. These configurations are shown in figure 4.8. Both symmetries have been observed in experiment with the adsorption energy of the $C_{3\nu}(\sigma_\nu)$ symmetry being 8% lower than for the $C_{3\nu}(\sigma_d)$ symmetry [1]. The following analysis focuses as a showcase on the $C_{3\nu}(\sigma_\nu)$ symmetry.

4.3.2 Supercell geometries

An adsorption energy calculation is usually based on three separate sub–calculations as is described in section 3.4. Each calculation uses a different supercell containing either the benzene at the surface, the clean Ag(111) surface, or the gas phase molecule (as depicted in figure 4.9). The geometries used here were provided by
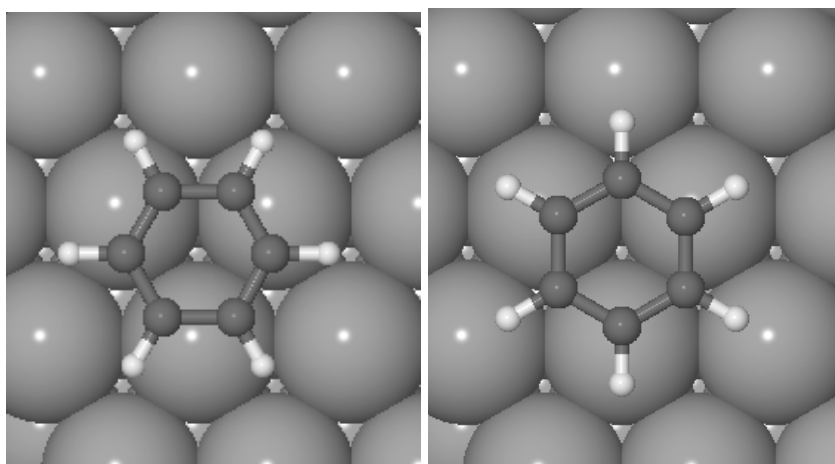
Figure 4.8: The $C_{3\nu}(\sigma_d)$ (left) and $C_{3\nu}(\sigma_\nu)$ (right) configuration of benzene on Ag(111)

Erik McNellis [34] and their convergence behaviour in terms of the non-vdW part of the calculation is already known [34].
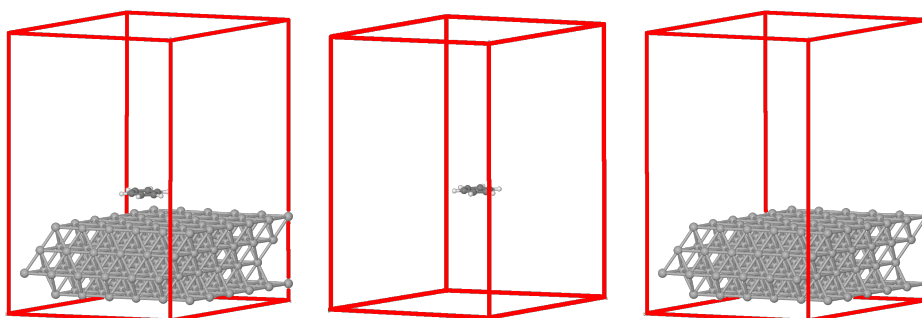
Figure 4.9: Benzene adsorption geometries in a 6×6 supercell

Since the aim is the simulation of a single benzene molecule at an infinitely extended surface, lateral interactions between adjacent molecules (due to the periodic repetition of the supercell) should be avoided. To verify this, two sets of supercells were used. One with a 6×6 slab geometry as shown in figure 4.9 and a smaller one with a 3×3 geometry. The gas phase reference was always obtained from the 6×6 sized supercell. One often finds that an even larger supercell is used for gas phase references, however the JuNoLo program which was used for the vdW-DF calculations can suffer from numerical inconsistencies—referred to

as the $\phi(0)$–issue in the JuNoLo Manual [35]—if the size of the supercells varies too much from geometry to geometry. For the same reason the benzene molecule was placed at the same position in both the gas phase reference supercell as well as the adsorption supercell.

All calculations were performed with the positions of the slab atoms fixed according to the bulk structure. The structure of the benzene molecule was relaxed using geometry optimization for both, the adsorbed as well as the gas phase structures. The DFT functional used was PBE.

4.3.3   Convergence

The convergence behaviour of the used geometries in the case of non-vdW DFT calculations using the PBE functional has already been investigated [34] and the same parameters will be used here. The smearing width was set to $80\,\mathrm{meV}$ and a $4 \times 4 \times 1$ Monkhorst Pack k-point grid was used. The number of slab layers is 4 with an overall supercell height of $30\,\mathrm{Å}$. The benzene–surface distance used here is the one predicted from GGA–DFT using the PBE functional.

Kinetic energy cutoff

The kinetic energy cutoff determines the number of density grid points available for the vdW-DF step (see also section 3.2.1). It is thus important to re–evaluate its influence on the final adsorption energy. The conclusion of this test is shown in figure 4.10. As one can see, the 3×3 geometry generally converges faster (at $500\,\mathrm{eV}$) than the 6×6 geometry (between $650\,\mathrm{eV}$ and $850\,\mathrm{eV}$). The difference between the two 3×3 curves lies in the way periodicity was treated where $p = 0$ means that no periodicity was used for the vdW-DF calculation, whereas $p = 1$ denotes a single repetition of the unit cell in each lateral direction

The non–periodic calculation is obviously not fully converged while the periodic one leads to about the same result as the 6×6 run. This also tells us that the periodic images of the benzene molecule in the 3×3 case don't suffer from any lateral interactions.

The reasons for the bad performance of the non–periodic 3×3 calculation is that the surface area underneath the adsorbed molecule is very small which limits the number of surface atoms that can be part of the vdW interaction. A
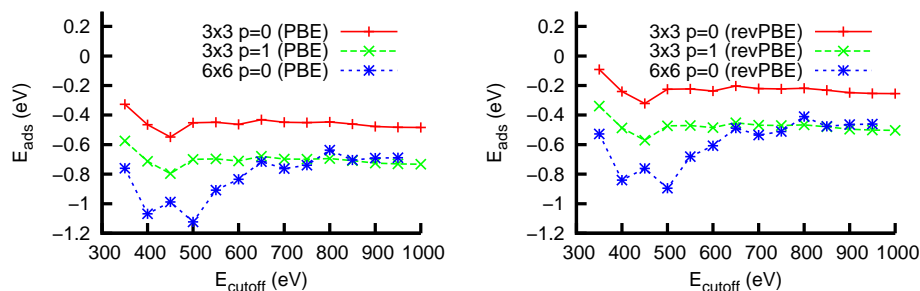
Figure 4.10: Convergence with kinetic energy cutoff for different supercell sizes and JuNoLo periodicity settings. $p = 0$ means that no periodicity was used for the vdW-DF calculation, whereas $p = 1$ denotes a single repetition of the unit cell in each lateral direction, so that one gets a 3×3 grid of unit cells.

wider surface area should increase the number and thus the strength of the vdW interaction, correcting the resulting energy downward.

Looking at the pure PBE results (before the vdW-DF correction is applied) in figure 4.11, we can see that convergence is reached immediately and that the slow convergence is solely caused by the vdW-DF part of the calculation.
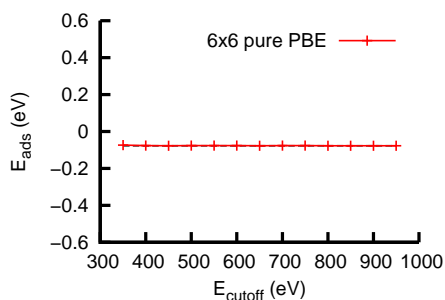
Figure 4.11: Convergence of the pure PBE part of the calculation with the kinetic energy cutoff.

The converged adsorption energies (with the substrate–adsorbate distance optimized via PBE) are shown in table 4.2

There are two general problems with these results: The kinetic energy cutoff of at least $500\,\text{eV}$ is already quite high (especially for the non–vdW calculation) and, while feasible for the mid–sized problem of adsorbed benzene, could be a

Geometry	Cutoff	E_{ads} PBE	E_{ads} revPBE
3×3	$500\,\mathrm{eV}$	$-0.69\,\mathrm{eV}$	$-0.47\,\mathrm{eV}$
6×6	$850\,\mathrm{eV}$	$-0.70\,\mathrm{eV}$	$-0.47\,\mathrm{eV}$

Table 4.2: Converged adsorption energy of benzene at Ag(111) with the substrate–adsorbate distance determined via PBE based geometry optimization

significant issue if one were to investigate larger systems. The required periodicity for the 3×3 supercell also results in a significant slowdown of the computation. It would thus be advantageous to find a way of improving the results so that a DFT calculation with a lower kinetic energy cutoff produces the same outcome. Possible approaches for this have been investigated in sections below.

Density trimming

JuNoLo offers an option called density trimming, which allows to reduce the number of density grid points taken into account by the calculation. This is done by ignoring points at which the density lies below a certain threshold. Of course, the results obtained in a calculation have to be converged concerning this threshold. As can be seen from figure 4.12, the adsorption energy is rather insensitive to this quantity and for future calculations a value of $2 \cdot 10^{-4}$ (a.u.) has been used.
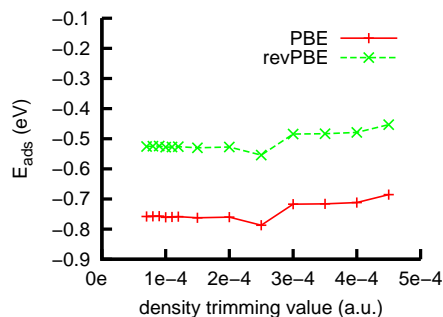

Figure 4.12: Convergence with JuNoLo density trimming.

4.3.4 Constant offset correction

One option to reduce the cost of the computation for obtaining a complete adsorption curve for benzene on Ag(111) is to use a constant offset to correct calculations performed with lower kinetic energy cutoff. It would then be sufficient to obtain one data point at high cutoff to find the required offset and get the rest of the curve using a lower cutoff. Of course, one first has to verify that the offset is approximately constant for different substrate–adsorbate distances. Since the JuNoLo calculations with the 6×6 cell are faster than the ones with 3×3 cell which requires periodicity, the 6×6 supercell was used for the following analysis.

Two additional convergence tests have been performed with the benzene molecule moved orthogonal to the surface either by 0.1 Å towards the surface (see figure 4.13) or by 1.0 Å away from the surface (see figure 4.14). The geometry of the benzene molecule itself was kept fixed in the PBE optimized state.

Both tests showed that the energy difference (i.e. the energy correction offset) is basically constant for both benzene positions over a wide range of the kinetic energy cutoff. The origin of the anomaly between 650 eV and 800 eV is not known, but expected to be caused by numerical problems in the JuNoLo code, possibly related to the $\phi(0)$–issue described in the JuNoLo manual [35]. It will be avoided in the following calculations by not using a kinetic energy cutoff in that range.

A comparison of two full adsorption curves with kinetic energy cutoffs of 350 eV and 850 eV can be seen in figure 4.17 in section 4.3.6. It is found that the offset stays constant over the whole range which allows the correction of the 350 eV curve by simply requiring it to reach zero for large adsorbate–substrate distances.

4.3.5 Interpolation

While the offset correction presented above already improves the situation quite a bit, it would be preferable if it was sufficient to do no high–cutoff calculation at all and to also avoid the additional calculation at large adsorbate–substrate distance. If the kinetic energy cutoff requirements of the vdW-DF calculation using JuNoLo were no higher than those required by the non–vdW calculation, it would be possible to reuse already existing electron densities from old simulations which employed local or semi-local functionals and add the vdW–DF correction as a pure

(a)

(b)

(c)

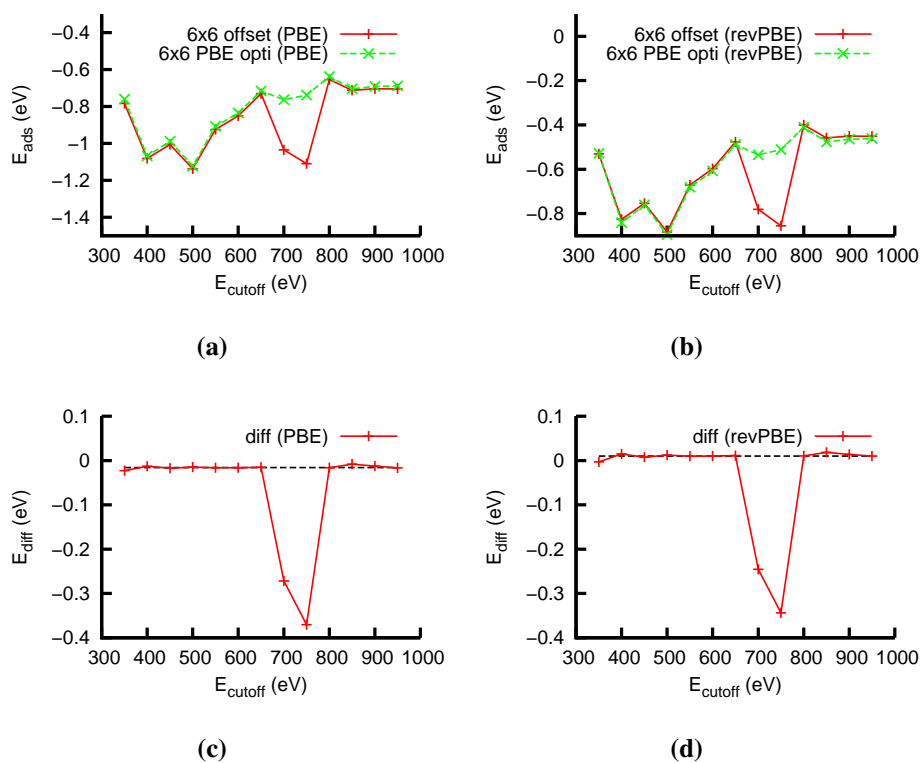**(d)**

Figure 4.13: Adsorption energy of benzene on Ag(111) with the molecule moved closer to the surface by $0.1\,\text{Å}$ compared to the position obtained from PBE based geometry optimization. (a) and (b) show the convergence with the kinetic energy cutoff for the PBE and revPBE functional respectively. (c) and (d) show the difference of the calculations with and without position offset.
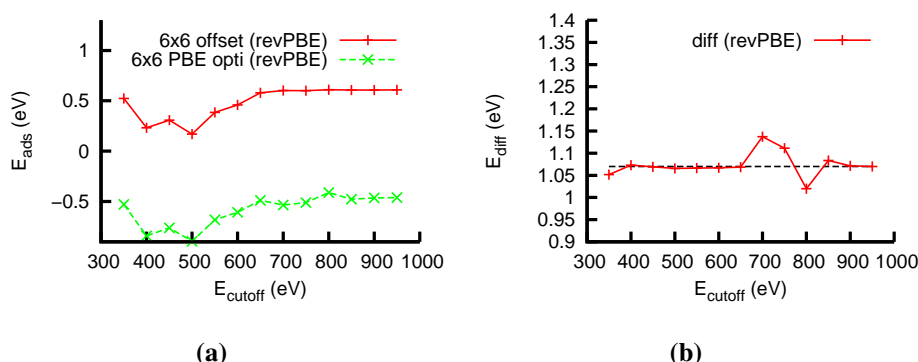
Figure 4.14: Adsorption energy of benzene on Ag(111) with the molecule moved away from the surface by $1.0\,\text{Å}$ compared to the position obtained from PBE based geometry optimization. (a) shows the convergence with the kinetic energy cutoff for revPBE, (b) the difference of the calculations with and without position offset.

post-processing step.

This option has been tested by using a spline interpolation applied to the density of the 6×6 geometry. To not lose any information present in the original density, the number of points was doubled in each direction, resulting in a new, interpolated point in between every pair of existing grid points. When starting from the $350\,\text{eV}$ density, this created a grid containing $215 \times 215 \times 383$ points, which is more than the $180 \times 180 \times 288$ resulting from a $850\,\text{eV}$ calculation. The results of this interpolation for the $350\,\text{eV}$ and $400\,\text{eV}$ input densities are listed in table 4.3.

Cutoff	Grid Size	E_{ads} with PBE	E_{ads} with revPBE
$350\,\text{eV}$	$108 \times 108 \times 192$	$-0.76\,\text{eV}$	$-0.53\,\text{eV}$
$400\,\text{eV}$	$120 \times 120 \times 200$	$-1.07\,\text{eV}$	$-0.84\,\text{eV}$
$350\,\text{eV}$	$215 \times 215 \times 383$	$-0.68\,\text{eV}$	$-0.45\,\text{eV}$
$400\,\text{eV}$	$239 \times 239 \times 399$	$-0.99\,\text{eV}$	$-0.76\,\text{eV}$

Table 4.3: Effect of density grid interpolation on the adsorption energy. The first two rows show the results obtained from the original densities.

While the interpolation correction of E_{ads} does go into the right direction, it is

still far away from the fully converged results from the $850\,\text{eV}$ cutoff calculation. This is especially obvious with the interpolation results obtained from the $400\,\text{eV}$ density.

4.3.6   Adsorption curve

The raw PBE adsorption curve is shown in figure 4.15. It is the starting point which is to be improved by the consideration of vdW interactions. The kinetic energy cutoff used was $E_{\text{cutoff}} = 850\,\text{eV}$ with the 6×6 geometry and all other convergence parameters as listed in section 4.3.3. The small binding which can be
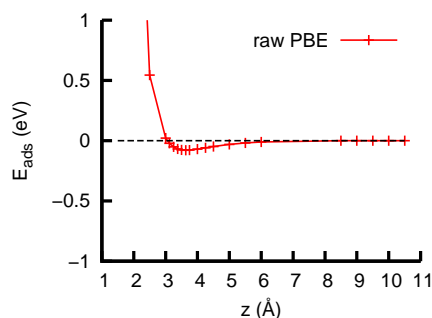

Figure 4.15: Raw PBE adsorption curve with $E_{\text{cutoff}} = 850\,\text{eV}$

observed even when using only the PBE functional has been shown [36] to stem mainly from the exchange part of the functional which is incorrect, as the van der Waals based binding in this system is predominantly a correlation phenomenon. The adsorption distance is measured from the center of mass of the benzene molecule to the atom cores of the first surface layer, with the PBE functional predicting a distance of $z_0 = 3.50\,\text{Å}$.

Adding the energy corrections obtained using the vdW-DF functional, one gets the adsorption curve shown in figure 4.16 which looks a lot more promising. The minima of both curves are listed in table 4.4. TPD experiments [1] yielded an adsorption energy of $(0.522 \pm 0.004)\,\text{eV}$.

Constant offset correction

It was shown in section 4.3.4 that the error introduced due to a small kinetic energy cutoff is constant over a wide range of adsorbate–substrate distances. It is
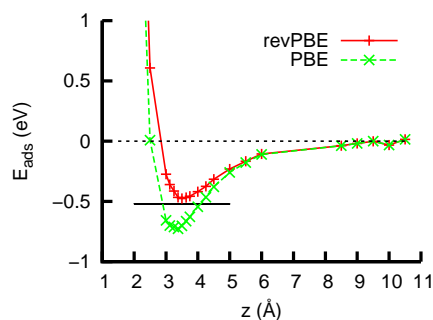
Figure 4.16: vdW-DF corrected adsorption curve for benzene on Ag(111). The experimentally determined [1] adsorption energy is marked with a black bar.

x-functional	E_{ads}	z_0
PBE	$-0.73\,\mathrm{eV}$	$3.38\,\text{Å}$
revPBE	$-0.47\,\mathrm{eV}$	$3.50\,\text{Å}$
Experiment [1]	$-0.522(4)\,\mathrm{eV}$	—

Table 4.4: Minima of the adsorption curves for different exchange functionals.

thus plaussible that one could perform the calculations at a lower, not converged, cutoff and shift the resulting adsorption curve by an offset. For this purpose, an additional adsorption curve was created with a kinetic energy cutoff of $350\,\mathrm{eV}$ (see figure 4.17). Since the offset between the two curves in figure 4.17a stays constant, the $350\,\mathrm{eV}$ calculation can be corrected by shifting it so that it reaches zero for long adsorbate–substrate distances. This basically means that the gas phase reference is replaced with a "pseudo gas phase" reference, where the benzene molecule is not placed in a separate supercell, but instead placed at a large distance to the surface slab.
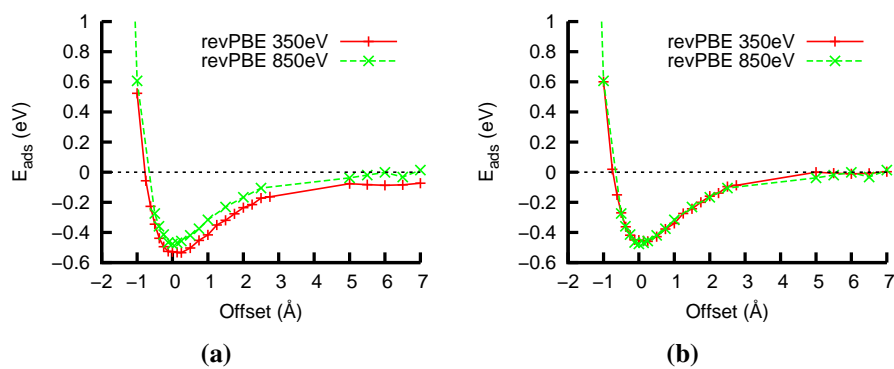
Figure 4.17: (a): Comparison of the adsorption curve with a kinetic energy cutoff of
850 eV and 350 eV. (b): The same comparison with the 350 eV curve
shifted.

Chapter 5

Conclusion

In the present study, the adsorption of benzene at Ag(111) was described quantitatively using the recently developed non–local vdW–DF functional with the obtained energies closely resembling experimental results.

In preceding studies [34], which relied on DFT-D schemes (such as the TS approach), the geometry of adsorbed molecules could already be predicted quite successfully. However, the predicted binding was far too strong, overbinding almost as much as GGA functionals underbind. It was suggested, that the overbinding results from electronic screening, an effect not accounted for in DFT-D. The vdW-DF functional used in this study, with its non–local structure, is capable of accounting for screening and is thus an option for improving the adsorption energy results.

The adsorption energy obtained in this work for the adsorbed benzene molecule successfully reproduces the experimental data with a theoretical value of $-0.47\,\mathrm{eV}$ compared to $-0.52\,\mathrm{eV}$ obtained from experiments. However, one major weakness of the employed approach turned out to be its reliance on the resolution of the electron density and with that, on the kinetic energy cutoff used for the calculations. The high cutoff value necessary for converged results requires extensive DFT calculations which are not feasible for large structures, such as azobenzene or PTCDA.

It was thus attempted to avoid this deficiency by either interpolating the electron density from the DFT calculation, or by finding a way to correct the results from lower cutoff calculations. While the interpolation method did not turn out

to be successful, it was possible to correct the low–cutoff results using a constant energy offset. By requiring the adsorption energy to reach zero for high adsorbate–substrate distances, this constant offset can be determined. This additionally reduces the computational cost as the gas phase reference is then replaced by a reference value obtained from this "high distance" calculation.

Using this low–cutoff based method, the simulation of larger structures is a logical next step. It would be especially interesting to see if the good geometry prediction using DFT-D schemes can be combined with the adsorption energy predicted by the vdW-DF functional. The geometry optimization would then be performed using DFT-D and the vdW-DF functional would continue to be used as a pure post–processing step for the already optimized geometries.

It should also be noted that new non–local functionals, which have a mathematical structure very similar to the vdW-DF functional used in this work, are already being developed [37]. Their integration into the framework presented here should be a viable option for further investigations.

Appendix A

Additional methods

A.1 Density stitching

Density Stitching is a method developed in the course of this work, but was later abandoned as it was not nececary for the simulation of the benzene adsorption. However, it might still be useful for the study of larger molecules which is why it is presented here. The aim of this method is to allow small supercells to be used (e.g. the 3×3 supercell from section 4.3.2) for the standard DFT calculation while at the same time avoiding lateral interactions between the periodic images of the adsorbates when using periodic boundary conditions in the vdW–DF code JuNoLo (where the long range vdW interactions can be much more of a problem).

If one did a vdW–DF calculation with a small supercell, but without periodicity, one often finds that the substrate area is too small to properly account for the vdW–interaction between an infinitely extended surface and the adsorbate. To solve this problem, two separate standard DFT calculations are performed with the supercells (and the resulting densities) shown in figure A.1: One with the adsorbate–substrate geometry and another one with only a clean surface in it.

The resulting electron densities are then stitched together laterally with one adsorbate–substrate density in the center surrounded by eight surface densities (see figure A.2). That way, one obtains a large supercell without lateral interactions for the (then non–periodic) JuNoLo calculation while maintaining fast standard DFT calculations with small supercells.
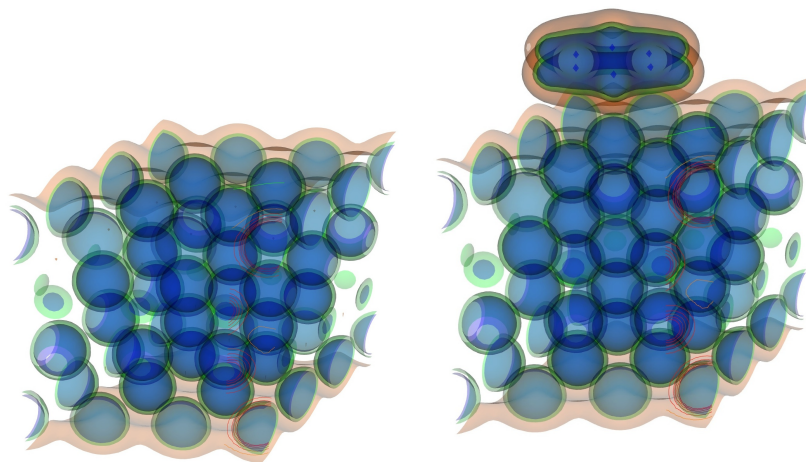
Figure A.1: Starting densities which are stitched together to form a larger density super-cell.
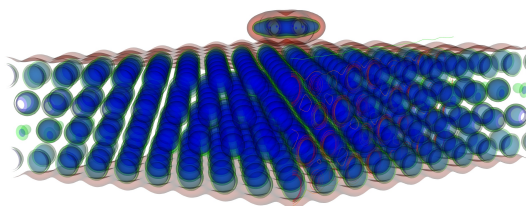

Figure A.2: Final stitched density for the vdW-DF calculation.

Bibliography

[1] T. J. Rockey, M. Yang, and H. Dai. Adsorption energies, inter-adsorbate interactions, and the two binding sites within monolayer benzene on ag(111). *J Phys Chem B*, 110(40):19973–8, 2006.

[2] W. Heitler and F. London. Wechselwirkung neutraler atome und homöopolare bindung nach der quantenmechanik. *Zeitschrift für Physik*, 44(6-7):455, 1927.

[3] C. J. Cramer. *Essentials of Computational Chemistry: Theories and Models*. Wiley, 2004.

[4] E. Hückel. Quantentheoretische beiträge zum benzolproblem. *Zeitschrift für Physik*, 70(3-4):204, 1931.

[5] P. Hohenberg and W. Kohn. Inhomogeneous electron gas. *Physical Review*, 136(3B):B864, 1964.

[6] W. Kohn and L. J. Sham. Self-consistent equations including exchange and correlation effects. *Physical Review*, 140(4A):A1133, 1965.

[7] R. G. Parr. Density-functional theory of the electronic structure of molecules. *Annual Review of Physical Chemistry*, 34(1):631, 1983.

[8] W. Kohn, A. D. Becke, and R. G. Parr. Density functional theory of electronic structure. *The Journal of Physical Chemistry*, 100(31):12974, 1996.

[9] E. H. Lieb. Thomas-fermi and related theories of atoms and molecules. *Reviews of Modern Physics*, 53(4):603, 1981.

[10] M. Dion, H. Rydberg, E. Schröder, D. Langreth, and B. Lundqvist. Van der waals density functional for general geometries. *Physical Review Letters*, 92(24):246401, 2004.

[11] T. Ikeda and O. Tsutsumi. Optical switching and image storage by means of azobenzene liquid-crystal films. *Science*, 268(5219):1873–5, 1995.

[12] L. Hung. Recent progress of molecular organic electroluminescent materials and devices. *Materials Science and Engineering: R: Reports*, 39(5-6):143, 2002.

[13] J. Perdew, K. Burke, and M. Ernzerhof. Generalized gradient approximation made simple. *Physical Review Letters*, 77(18):3865, 1996.

[14] Y. Zhang and W. Yang. Comment on "generalized gradient approximation made simple". *Physical Review Letters*, 80(4):890, 1998.

[15] E. H. Lieb and S. Oxford. Improved lower bound on the indirect coulomb energy. *International Journal of Quantum Chemistry*, 19(3):427, 1981.

[16] Q. Wu and W. Yang. Empirical correction to density functional theory for van der waals interactions. *The Journal of Chemical Physics*, 116(2):515, 2002.

[17] S. Grimme. Accurate description of van der waals complexes by density functional theory including empirical corrections. *Journal of Computational Chemistry*, 25(12):1463, 2004.

[18] A. Tkatchenko and M. Scheffler. Accurate molecular van der waals interactions from ground-state electron density and free-atom reference data. *Physical Review Letters*, 102(7):073005, 2009.

[19] H. Rydberg, B. Lundqvist, D. Langreth, and M. Dion. Tractable nonlocal correlation density functionals for flat surfaces and slabs. *Physical Review B*, 62(11):6997, 2000.

[20] H. Rydberg, M. Dion, N. Jacobson, E. Schröder, P. Hyldgaard, S. Simak, D. Langreth, and B. Lundqvist. Van der waals density functional for layered structures. *Physical Review Letters*, 91(12):126402, 2003.

[21] D. C. Langreth, M. Dion, H. Rydberg, E. Schröder, P. Hyldgaard, and B. I. Lundqvist. Van der waals density functional theory with applications. *International Journal of Quantum Chemistry*, 101(5):599, 2004.

[22] M. Dion. *Van der Waals forces in density functional theory*. PhD thesis, Rutgers University, 2004.

[23] D. Langreth and J. Perdew. Exchange-correlation energy of a metallic surface: Wave-vector analysis. *Physical Review B*, 15(6):2884, 1977.

[24] H. J. Monkhorst and J. D. Pack. Special points for brillouin-zone integrations. *Physical Review B*, 1976.

[25] B. Meyer. *Computer Nanoscience: Do It Yourself!*, volume 31 of *NIC Series*, chapter The Pseudopotential Plane Wave Approach, pages 71–83. John von Neumann Institute for Computing, 2006.

[26] S. J. Clark, M. D. Segall, C. J. Pickard, P. J. Hasnip, M. I. J. Probert, K. Refson, and M. C. Payne. First principles methods using castep. *Zeitschrift für Kristallographie*, 220(5-6):567–570, 2005.

[27] T. Thonhauser, V. R. Cooper, S. Li, A. Puzder, P. Hyldgaard, and D. C. Langreth. Van der waals density functional: Self-consistent potential and the nature of the van der waals bond. *Physical Review B*, 76(12):125112, 2007.

[28] P. Lazić, N. Atodiresei, M. Alaei, V. Caciuc, S. Blügel, and R. Brako. Junolo – jülich nonlocal code for parallel post-processing evaluation of vdw-df correlation energy. *Computer Physics Communications*, 181(2):371, 2010.

[29] F. D. Murnaghan. The compressibility of media under extreme pressures. *Proc Natl Acad Sci U S A*, 30(9):244–247, 1944.

[30] J. L.F. Da Silva, C. Stampfl, and M. Scheffler. Converged properties of clean metal surfaces by all-electron first-principles calculations. *Surface Science*, 600(3):703, 2006.

[31] A. Michaelides and M. Scheffler. *Textbook of Surface and Interface Science*, volume 1, chapter An Introduction to the Theory of Metal Surfaces. Wiley-VCH, 2010.

[32] N. Takeuchi, C. Chan, and K. Ho. Au(111): A theoretical study of the surface reconstruction and the surface electronic structure. *Physical Review B*, 43(17):13899, 1991.

[33] A. Anderson, M. McDevitt, and F. Urbach. Structure and electronic factors in benzene coordination to cr(co)3 and to cluster models of ni, pt, and ag (111) surfaces. *Surface Science*, 146(1):80, 1984.

[34] E. R. McNellis. *First-Principles Modeling of Molecular Switches at Surfaces*. PhD thesis, 2009.

[35] P. Lazić. *JuNoLo Program Manual*, 2008.

[36] X. Wu, M. C. Vargas, S. Nayak, V. Lotrich, and G. Scoles. Towards extending the applicability of density functional theory to weakly bound systems. *The Journal of Chemical Physics*, 115(19):8748, 2001.

[37] O. Vydrov and T. Van Voorhis. Nonlocal van der waals density functional made simple. *Physical Review Letters*, 103(6):063004, 2009.